



Tailored Pd/C bifunctional catalysts for styrene production under an ethylbenzene oxidative dehydrogenation assisted direct dehydrogenation scheme

Xueya Dai^{a,b}, Tianlong Cao^a, Xingyu Lu^{a,b}, Yunli Bai^{a,b}, Wei Qi^{a,b,*}

^a Shenyang National Laboratory for Materials Science, Institute of Metal Research, Chinese Academy of Sciences, Shenyang 110016, People's Republic of China

^b School of Materials Science and Engineering, University of Science and Technology of China, Shenyang 110016, People's Republic of China

ARTICLE INFO

Keywords:

Pd single atom
Nanocarbon
Bifunctional catalyst
Oxidative dehydrogenation
Direct dehydrogenation

ABSTRACT

Rational design of efficient ethylbenzene (EB) dehydrogenation catalyst and reaction route is the key scientific challenge for styrene (ST) formation. We reported here a dual-path dehydrogenation (DPDH) route to efficiently convert EB to ST on a Pd/hollow nanocarbon spheres bifunctional catalyst, which exhibited ST formation rate up to 7.11 mmol g⁻¹ h⁻¹ with > 99 % selectivity. Detailed kinetic, isotopic and surface reaction analysis and corresponding DFT calculation suggested that the relatively high intrinsic catalytic activity originated not only from the single atomically dispersed Pd-based coordination structure but also the unique oxidative dehydrogenation (ODH) assisted direct dehydrogenation (DDH) reaction route. In this route, the small amount of H₂O produced from ODH effectively lowered the energy barrier for hydrogen generation/desorption via a proton transfer process promoting the DDH process. The present work shed light on the rational design of catalyst and routes for highly efficient alkane dehydrogenation reaction systems.

1. Introduction

The annual global production of styrene (ST), which is considered as one of the most widely applied chemical feedstock for polymer industry, exceeds 30 million tons resulting an annual CO₂ emission over 27 million tons per year [1–3]. The application of noble metal catalysts in alkane dehydrogenation is still restricted by their low efficiency, stability and limited resources, although Pt or Pd exhibits very high activity in direct dehydrogenation (DDH) of ethylbenzene (EB) for ST synthesis. Potassium-promoted iron oxide is currently serving as the typical commercial catalyst for EB DDH, and it also faces the severe problems of carbon deposition and deactivation etc. With the unparalleled development of nanotechnology and novel synthetic techniques, metal single atoms (SAs), which have shown the theoretically largest number of exposed active sites and unique physical-chemical properties, become one of the most sophisticated frontiers in the field of catalysis and chemical engineering [4–6]. Noble metal SAs catalyzing EB dehydrogenation normally follows DDH route and has shown multiple advantages including the unique reaction pathway [7–10], low adsorption/activation energy [11,12] and high selectivity of alkene [13,

14], low carbon deposition [12] and maximal atom utilization efficiency [15,16] etc. However, the EB DDH process still encounters severe problems of low activity and high reaction temperature for its highly endothermic nature requesting excess superheated-steam protection and relatively high reaction temperature (normally at around 650 °C), which can not meet the urgent demanding concept of energy conservation and sustainable chemistry. In addition, EB DDH on noble metal also suffers from carbonaceous deposit due to the equilibrium-limited incomplete desorption and polymerization of ST, which brings serious problems of catalyst deactivation and difficulties in regeneration.

EB oxidative dehydrogenation (ODH) reaction, especially ODH reaction on green and renewable nanocarbon catalysts, is believed as a promising alternative route for ST synthesis showing great potential due to its unique advantages of non-equilibrium limitation, high ST selectivity, low reaction temperature and free of carbonaceous deposition [17]. The key scientific challenge for carbon catalyzed alkane ODH reaction is the improvement of the intrinsic catalytic activity of carbon and the control of the oxygen dosage, ensuring the high alkene selectivity and oxidation stability of the reaction system. Rational design of the catalyst system and proper choice of the reaction condition that

* Corresponding author at: Shenyang National Laboratory for Materials Science, Institute of Metal Research, Chinese Academy of Sciences, Shenyang 110016, People's Republic of China.

E-mail address: wqi@imr.ac.cn (W. Qi).

<https://doi.org/10.1016/j.apcatb.2022.122205>

Received 23 September 2022; Received in revised form 18 November 2022; Accepted 21 November 2022

Available online 22 November 2022

0926-3373/© 2022 Elsevier B.V. All rights reserved.

synergizing the DDH and ODH process is one of the most possible solutions for efficient ST production.

Nanocarbon material with tunable surface properties and compositions is one of the most ideal supports for SAs, since the strong chemical bonding/interactions between carbon and SAs would generate efficient charge transfer, which not only decreases the surface free energy thus achieving appreciable stability but also strongly improves the catalytic activity of SAs [17–25]. Inspired by the novel fabrication procedure of SA/nanocarbon hybrid materials, we proposed a Pd SAs/nitrogen-doped-carbon hollow nanospheres (Pd@HNSs) bifunctional catalyst in the present work, in which Pd SAs are supported on nanocarbon and stabilized by nitrogen/oxygen atoms. Pd@HNSs can simultaneously catalyze EB DDH and ODH reactions, and this dual-path dehydrogenation (DPDH) route is not the simple sum but the synergy of DDH and ODH process, exhibiting the advantages of high activity and selectivity, low reaction temperature and high stability etc. The proposed Pd@HNSs catalyzed EB DPDH process exhibited ST formation rate of $7.11 \text{ mmol g}^{-1} \text{ h}^{-1}$ with over 99 % selectivity, which is superior to most of the typical ST synthesis system. EB ODH process was found happened on ketonic carbonyl ($\text{C}=\text{O}$) groups on HNSs, and DDH reaction occurred on Pd single atoms. EB ODH, which is triggered by small amount of O_2 (five times lower than stoichiometry), does not only provide extra heat for the endothermic DDH reaction but also yield small amount of H_2O that concomitantly enhance the DDH activity by facilitating the H_2 desorption step via a water assisted proton transfer process. The proposed DPDH reaction route can convert EB at relatively low temperature, exhibiting high ST selectivity, stability and the superheated-steam free nature, showing its great potential for practical applications. The physical-chemical nature for the ODH assisted DDH approach, which was discovered on SAs/nanocarbon hybrid catalyst for the first time, may shed light on the rational design of catalysts and proper choice of reaction conditions towards highly efficient alkene production systems via alkane dehydrogenation route.

2. Experimental

2.1. Materials

The dopamine hydrochloride (DA, >98.0 %) was purchased from Sigma Aldrich and was used as received. The $\text{Pd}(\text{NO}_3)_2$ (>99 %) was purchased from InnoChem. The ethanol (>99.7 %, EA) was purchased from Tianjin Fuyu Fine Chemical Co., Ltd. The ethylbenzene (>99.7 %, EB) was purchased from Sigma Aldrich. The deuterated ethylbenzene (>99 %, C_8D_{10}) was purchased from Sigma Aldrich. The other reagents were purchased from Sino-pharm Chemical Reagent Co., Ltd and were used as received. The O_2 (99.999 %), He (99.999 %) and Ar (99.999 %) were purchased from Dalian Special Gases Co., Ltd.

2.2. Preparation of Pd@HNSs

In a typical experiment for synthesizing SiO_2 spheres, the ammonia aqueous solution (21 mL, 25–28 %) was mixed with ethanol (350 mL) and deionized water (7 mL) with stirring at room temperature. 7 mL of tetraethyl orthosilicate (TEOS) was added into the above solution, and the mixture was stirred for 6 h to get SiO_2 nanospheres. The resulted SiO_2 nanospheres were separated by centrifugation and then dispersed in deionized water (220 mL) by ultrasonication for 30 min. Dopamine hydrochloride (1.6 g), ammonia aqueous solution (2 mL, 25–28 %) and $\text{Pd}(\text{NO}_3)_2$ solution (2 mL, containing 2 mg/mL Pd, stabilized by 0.5 vol% HNO_3) were added into the above (SiO_2 spheres) solution, and the mixture were then stirred for 24 h. The resulted SiO_2 @PDA nanospheres were separated by centrifugation and washed with deionized water for three times. The obtained SiO_2 @PDA was then dried in a drying oven at 80°C for 24 h and was carbonized at 600°C for 2 h under flowing argon atmosphere. The obtained black powder was leached sequentially in a 2 mol/L NaOH solution at 80°C for 6 h and then in a 0.5 mol/L HCl

solution at 80°C for 3 h to degrade and eliminate the SiO_2 cores. The mixture was filtered, and then the solid was washed with deionized water until the pH of the filtrate reached neutral, and the obtained sample was dried and labeled as Pd@HNSs. The HNSs was also synthesized for control experiments following the same procedure as above in the absence of $\text{Pd}(\text{NO}_3)_2$.

2.3. Characterizations

Inductively coupled plasma optical emission spectroscopy (ICP-OES) was measured by Agilent 730. The X-ray photoelectron spectra (XPS) were recorded with an ultra-high vacuum (UHV) ESCALAB 250 system equipped with a monochromatic Al $\text{K}\alpha$ X-ray source. The XRD patterns were collected on a Bruker D8 ADVANCE diffractometer with $\text{Cu-K}\alpha$ radiation. The N_2 adsorption-desorption isotherms were carried out with a Micrometrics ASAP 3020 instrument. The Raman experiments were measured on a HORIBA LabRam HR800 Raman spectrometer equipped with a laser source at a wavelength of 532 nm. IR studies were conducted with a Thermo Fisher Nicolet iS10 FT-IR system. The on-line off gas analysis was carried out in He with a Pfeiffer Omnistar mass spectrometer. The thermogravimetric analysis was performed on NETZSCH STA 449 C with temperature in the range of 40 – 900°C in Ar. The X-ray absorption fine structure spectra (XAFS) Pd K-edge were collected at beamline of the Australian Synchrotron (ANSTO). The data were collected in fluorescence mode using a Lytle detector while the corresponding reference samples were collected in transmission mode. The samples were grinded and uniformly daubed on the special adhesive tape. The data of XANES and EXAFS were analyzed by Athena software. TEM analysis was performed using FEI Tecna G2 T12 microscope with an accelerating voltage of 120 kV. High angle annular dark field scanning TEM (HAADF-STEM) images were recorded on a FEI Talos F200S G2 microscope. In-situ IR spectra analysis was conducted with a Thermo Fisher Scientific Nicolet iZ10 FT-IR spectroscopy equipped with a sample chamber. The Pd@HNSs sample was first diluted by abundant KBr to a light gray color and loaded into the in-situ chamber. EB vapor was then introduced into the chamber for 60 min, following He sweep. The in-situ chamber was raised from 100° to 500°C ($10^\circ\text{C}/\text{min}$) and TPRS-FTIR scans were collected. Isothermal FT-IR was conducted at 500°C . FT-IR scans were collected after EB vapor introduced. KBr at corresponding temperature were used as the background.

2.4. Ethylbenzene dehydrogenation reaction activity measurement

The EB dehydrogenation (DH) and dual-path dehydrogenation (DPDH) reactions were performed with 50 mg catalyst at desired temperature using a fixed-bed microreactor with He plug-flow. The molar flow rates of the reactant mixture (EB, O_2 and He) were adjusted for the desired EB and O_2 partial pressures (0.5–16 kPa for EB, 0–0.5 kPa for O_2). The deuterated ethyl benzene (D-EB) used in the kinetic isotope effect (KIE) test was fully deuterated EB with 99 % D abundance. The reactant and product concentrations were measured on-line with a gas chromatography (GC, Agilent 7890 A) equipped with both flame ionization detector (FID) and thermal conductivity detector (TCD). A methyl silicone capillary column (HP-5) was connected to FID, and two Porapak Qpacked columns and a Sieve 5 A column were connected to TCD. The carbon balance of the reaction system was $100 \pm 5\%$ (the error may mainly come from the reactant introduction and gasification process and the product quantification process).

The isotopic exchange experiment was conducted under the same conditions as DPDH besides with co-feeding of EB and D-EB (1:1). The deuterated styrene products were detected and quantified by mass spectroscopy with m/z in the range of 104–112, corresponding to $\text{C}_8\text{H}_{8-x}\text{D}_x$ ($x = 0, 1, 2, 3, 4, 5, 6, 7, 8$), respectively. The $\text{C}_8\text{H}_6\text{D}_2$ shared similar $m/z = 106$ value as C_8H_{10} , and thus the distribution of $\text{C}_8\text{H}_6\text{D}_2$ was not analyzed.

2.5. Computational details

The first-principles were employed to perform all spin-polarization density functional theory (DFT) calculations within the generalized gradient approximation (GGA) using the Perdew-Burke-Ernzerhof (PBE) formulation [26–28]. The projected augmented wave (PAW) potentials were chosen to describe the ionic cores, which also took valence electrons into account using a plane wave basis set with a kinetic energy cutoff of 450 eV [29,30]. Partial occupancies of the Kohn–Sham orbitals were allowed using the Gaussian smearing method with a width of 0.05 eV. The electronic energy was considered self-consistent when the energy change was smaller than 10^{-4} eV. A geometry optimization was considered convergent when the energy change was smaller than 0.05 eV \AA^{-1} . Finally, the adsorption energies (E_{ads}) were calculated as following equation:

$$E_{\text{ads}} = E_{\text{ad/sub}} - E_{\text{ad}} - E_{\text{sub}}$$

where $E_{\text{ad/sub}}$, E_{ad} , and E_{sub} were the total energies of the optimized adsorbate/substrate system, the adsorbate in the gas phase, and the clean substrate, respectively. The Brillouin zone integral used the surface structure of $3 \times 3 \times 1$ monkhorst pack K point sampling for PdN_3 -C structure. The free energy (ΔG) for elemental reaction steps were calculated as:

$$\Delta G = \Delta E + \Delta \text{EZPE} - T\Delta S$$

where ΔE was the difference between the total energy, ΔEZPE and

ΔS were the differences in the zero-point energy and the change of entropy, T was the temperature ($T = 300$ K in this work), respectively.

3. Results and discussions

3.1. Synthesis and chemical structure of Pd@HNSs

As shown in Fig. 1a, the proposed $\text{Pd@nitrogen-doped-carbon}$ hollow nanospheres (Pd@HNSs) hybrid catalysts were synthesized via the combination of pre-self-assembly, pyrolysis and subsequent leaching processes. Thin polydopamine shells were firstly decorated on the surface of SiO_2 nanospheres via in situ polymerization in the aqueous solution of $\text{Pd}(\text{NO}_3)_2$ and ammonia, and the composite was separated via centrifugation, which was further pyrolyzed at 600°C , and the Pd@HNSs catalysts were obtained after removal of SiO_2 hard templates. Pd@HNSs also exhibited the same spherical morphology as that before removing SiO_2 core as shown in the SEM images in Fig. S1. Pure HNSs without Pd species were also synthesized following the similar procedure for comparisons except for the absence of $\text{Pd}(\text{NO}_3)_2$ in solution. The XPS survey spectra (Fig. S2a) demonstrated that C, N and O were three main elements without any other impurities on the surface of synthesized HNS samples. Adjacent hydroxyl ($-\text{OH}$) groups on dopamine monomer could transform into $-\text{C}=\text{O}$ sites, namely quinone functionalities after the polymerization and carbonization process (as shown in FT-IR results in Fig. S2b), which served as active sites for EB ODH reactions [31,32]. The accurate content of $-\text{C}=\text{O}$ groups on HNSs and

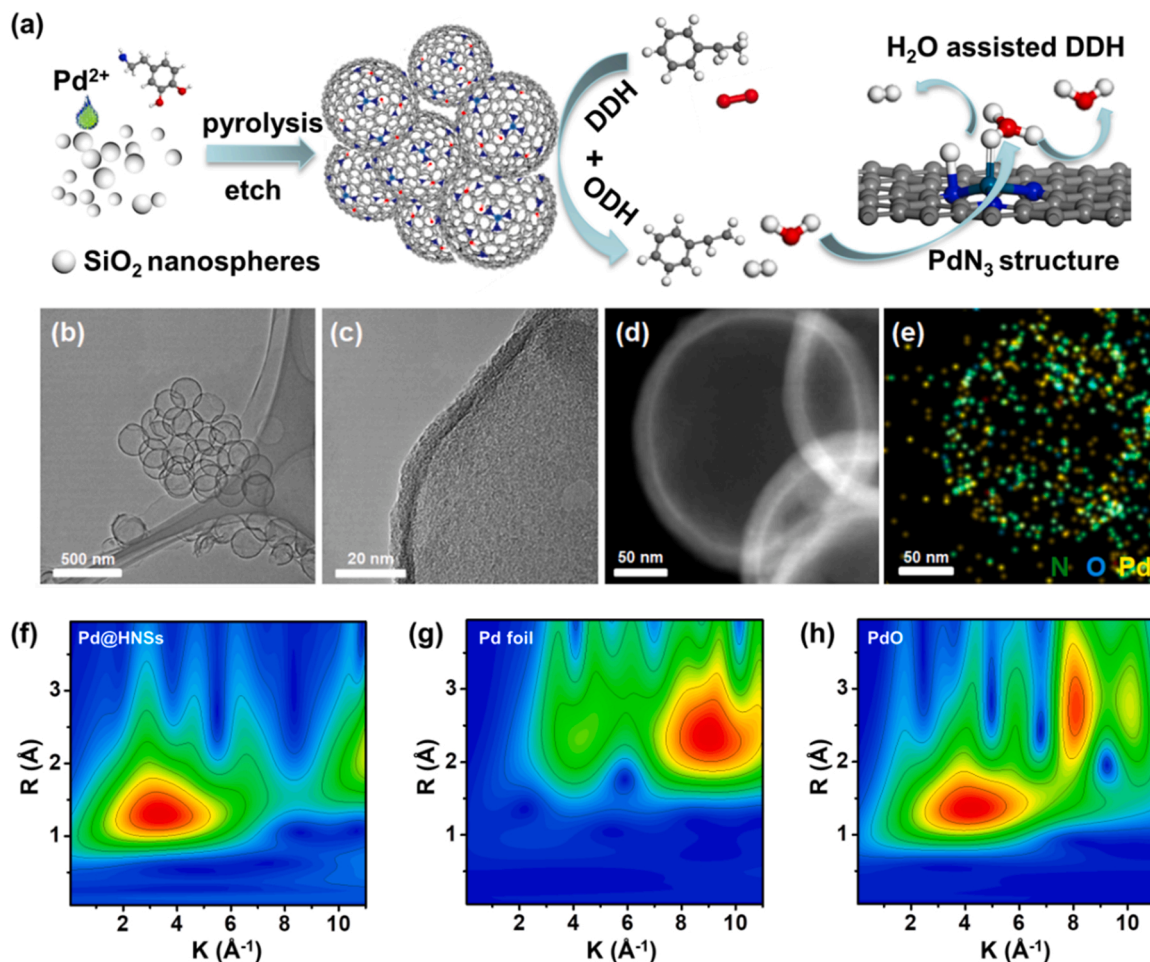


Fig. 1. (a) Schematic illustration for the preparation procedure of Pd@HNSs catalyst and the proposed EB DPDH route with corresponding H_2O assisted DDH process over Pd@HNSs . (b) and (c) TEM image, (d) HAADF-STEM image, (e) EDX mapping of Pd@HNSs . Wavelet transforms (WT) analysis of (f) Pd@HNSs , (g) Pd foil and (h) PdO.

Pd@HNSs was determined as 2.8 at% based on O 1 s XPS analysis (Fig. S3a and Table S1). On the other hand, the nitrogen containing groups on polydopamine enable strong absorption of Pd^{2+} via coordination interactions forming highly dispersed single-atom sites, and the Pd SAs can serve as the efficient active sites for EB DDH reactions. The total content of N element in HNSs and Pd@HNSs were determined as high as 8.2 at% and 7.5 at%, respectively, in which quaternary N took account for over 35 % (Fig. S3b and Table S1), which had shown prominent promotion effect for alkane ODH and DDH reactions [18,33]. The powder X-ray diffraction (XRD) patterns (Fig. S2c) exhibited no diffraction signals corresponding to Pd particles or other Pd compounds in Pd@HNSs, confirming the highly dispersed state of Pd element.

The transmission electron microscopy (TEM) images (Fig. 1b-c) suggested that the synthesized Pd@HNSs samples exhibited as a homogeneously distributed hollow nanosphere shape with the mean diameter of ~ 280 nm and the wall thickness of 10 nm. The elemental mapping analysis also testified the homogeneous distribution of the Pd, N and O elements in carbon matrix (Fig. 1d-e). Wavelet transform (WT) of Pd L_3 -edge extended X-ray absorption fine structure (EXAFS) oscillations showed visually the atomic dispersion of Pd throughout the whole catalyst (Fig. 1f-h). The hollow nanosphere structure induced the high Brunauer-Emmett-Teller (BET) surface area of HNSs and Pd@HNSs (1131 and 1108 $\text{m}^2 \text{g}^{-1}$, respectively) based on nitrogen adsorption/desorption isotherms (Fig. S2d, Table S1), and this relatively high surface area could benefit the heterogeneous catalytic reaction from the viewpoint of efficient mass transfer. Raman analysis (Fig. S2e) showed that the peak area ratio of D_1 band at 1340 cm^{-1} and G band at 1590 cm^{-1} (I_{D1}/I_G) for HNSs and Pd@HNSs samples were almost identical ($I_{D1}/I_G = 1.04$ vs. 1.07), indicating the similar defect structure of these two samples. The thermogravimetric analysis result (Fig. S2f) showed that both HNSs and Pd@HNSs were stable below 600°C [18].

The loading content of Pd in Pd@HNSs was detected at 0.51 wt% via inductively coupled plasma optical emission spectroscopy (ICP-OES) measurement, and which is slightly lower than that from XPS measurement (0.75 wt%). The local chemical state and coordination environment of Pd was revealed by X-ray adsorption fine structure (XAFS) analysis with Pd foil and PdO as references. As shown in the X-ray absorption near edge structure (XANES) spectroscopy (Fig. 2a), the valence state of Pd was found in between 0 and +2, indicating the slightly positively charged Pd species in Pd@HNSs. The Fourier-transformed (FT) k^2 -weighted extended X-ray absorption fine structure (EXAFS) of the Pd@HNSs (Fig. 2b) exhibited only a main peak at $\sim 1.5 \text{ \AA}$, corresponding to the first coordination shell of Pd in the bonding configuration of Pd-N [34–36]. WT plots of Pd@HNSs exhibited one maximum near 1.5 \AA , which should also be associated with single atomic Pd coordinated with N or O atoms. These results further confirmed the formation of Pd SAs on HNSs. The best fitting result of the EXAFS data (Fig. 2c) and its corresponding structure parameters (Table S2) revealed that the coordination number of the Pd is around 2.9, and the mean bond length between Pd and its coordinated atom is 1.97 \AA . It needs to be pointed out that it is quite difficult to distinguish Pd-N, Pd-O and even Pd-C via EXAFS result due to their similar bond length, suggesting the possible $\text{Pd-C}_x\text{N}_y\text{O}_z$ ($x + y + z = 3$) coordination structure in the fabricated Pd@HNSs catalyst [37]. However, Pd- N_3 is normally suggested as the representative structure existing in the sample from similar synthetic procedure due to the relatively strong coordination ability of nitrogen atoms [38–41]. Taking Pd- N_3 structure as an example, Fig. 2d exhibited the optimized structure of Pd- N_3 -Graphene (Pd- N_3 -Gr) based on DFT calculations and the corresponding charge density distribution analysis, which suggested that the delocalized electrons of Pd transferred to both N and surrounded C atoms, stabilizing the structure efficiently. The Bader charge of Pd and N was

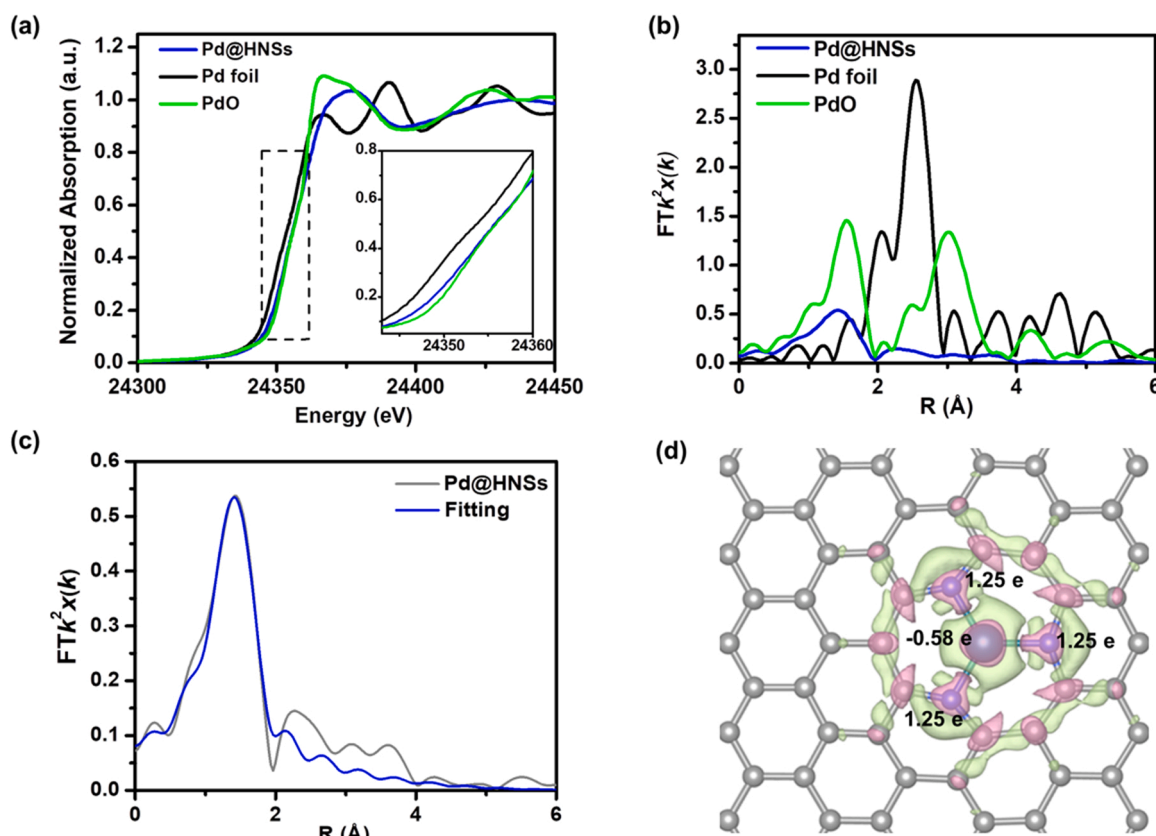


Fig. 2. (a) Normalized Pd K-edge XANES spectra and (b) Fourier-transformed Pd K-edge EXAFS spectra of the Pd@HNSs with the reference of Pd foil and PdO. (c) Corresponding EXAFS fitting curves of Pd@HNSs. (d) Calculated charge density distribution for the PdN₃ structure. The pink and green regions represent the areas of electron accumulation and loss, respectively.

determined at -0.58 e and 1.25 e, respectively, indicating the strong metal-support interactions.

3.2. ODH assisted DDH dual-path dehydrogenation of EB on Pd@HNSs

One of the key advantages of the proposed dual-path dehydrogenation (DPDH) process is the relatively low O_2 dosage in the reaction system. For example, O_2 to EB partial pressure ratio at 10 ($EB/O_2=10$) is determined as the optimized reaction condition for DPDH via screening the control experiments (as shown in Table S3), that can well balance the EB conversion and ST selectivity. This O_2 to EB partial pressure ratio is five times lower than the stoichiometry of EB ODH reaction, and the relatively low oxygen content benefits the oxidation stability of the reaction system, which can also meet the requirement of practical applications. In addition, the DPDH process for ST production avoids the shortcomings of EB DH and ODH reactions and exhibits the advantages in high activity and selectivity and low reaction temperature in the absence of steam protection as shown in Fig. 3a, which originates from the unique Pd@HNSs catalyst with DH and ODH bifunctional activity. As shown in Fig. 3b, EB DDH conversion on HNSs catalyst was only 3.7 %, whereas EB conversion increased over three times on Pd@HNSs reaching 10.4 % with over 99 % ST selectivity under the same reaction conditions, indicating that the Pd-based coordination structure contributed to most of EB DDH activity. Both HNSs and Pd@HNSs catalysts exhibited obvious enhancement of EB conversion from 3.7 % to 9.9 % and 10.4 % to 19.4 % upon switching DDH to DPDH ($EB/O_2=10$), suggesting that the introduction of small amount of O_2 benefited the ODH process on HNSs. Both DDH and DPDH route showed very low activity in EB conversion (<1.0 %, as shown in Fig. S4) in a typical blank experiment (without catalyst).

It can be observed from the time of stream diagram (EB conversion as

a function of reaction time) in Fig. 3b that HNS took less time to reach steady state in DDH than in DPDH route, which should be due to the rearrangement of surface oxygen functionalities in the presence of O_2 [42,43]. The slight decrease of the catalytic activity during this initial induction period was ascribed to the consumption (desorption) of oxygen functionalities, especially $-C=O$ groups as indicated by XPS analysis result (decreasing from 2.8 to 1.3 and 0.8 at% as shown in Fig. S5), indicating that $-C=O$ groups may directly relate to the ODH activity [42–44].

The enhancement of EB dehydrogenation activity in DPDH process stems from the switch of the reaction route, which effectively lowers the activation energy of the reaction as shown in Fig. 3c. DPDH on Pd@HNSs exhibited much lower apparent activation energy (45.4 kJ/mol) than DDH on Pd@HNSs (79.9 kJ/mol) and HNSs (96.0 kJ/mol). Matching DPDH route with bifunctional Pd@HNSs catalyst and the resulted activity improvement indicated the synergistic effect within ODH and DDH reactions instead of two independent reaction processes. Poor Arrhenius fitting of DPDH route on HNSs suggested that the ODH and DDH reaction may occur independently on HNSs (Fig. S6), in which case the reaction temperature had shown different effect on ODH and DDH reaction rate. The ST formation rate on Pd@HNSs in DPDH route was determined at $1.57 \text{ mmol g}^{-1} \text{ h}^{-1}$ at 2 kPa EB, and this value increased linearly with EB partial pressures in a relatively wide range (0.5–12 kPa) as shown in Fig. S7, suggesting that the reaction rate is kinetically controlled by the activation of EB. This hypothesis is well testified by kinetic isotope effect (KIE) experiment for ST (D-ST) formation rates of EB (C_8H_{10}) and deuterated EB (D-EB, C_8D_{10}) in DPDH on Pd@HNSs (Fig. 3d). The KIE values were determined to be 1.0–1.3, indicating that C-H bond activation is the rate-determining step under the chosen reaction conditions for DPDH.

The catalytic activity of Pd@HNSs for ST formation under DPDH

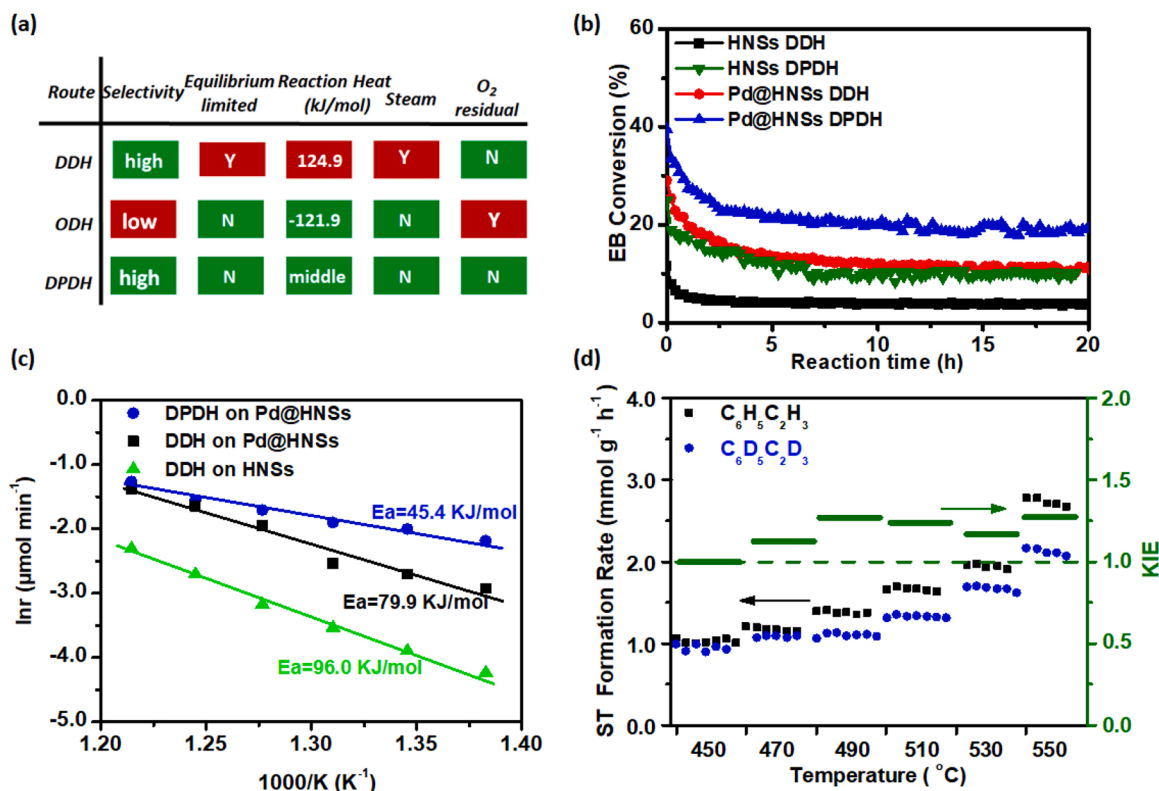


Fig. 3. (a) Comparisons of EB DDH, ODH and DPDH routes. Green background stands for desirable features or advantages, while the red background means the opposite. Y represents yes/with, while N represents no/without. (b) EB conversion as a function of reaction time on HNSs or Pd@HNSs in different routes. (c) Arrhenius plot for the HNSs and Pd@HNSs catalyzed reactions. (d) KIE of ST formation rate for the Pd@HNSs catalyzed DPDH reaction.

DDH reaction conditions: 50 mg catalyst, $500^{\circ}C$, 2 kPa EB, 7.65 mL/min in He. DPDH reaction conditions: all the reaction conditions were kept the same as DDH besides co-feeding O_2 at $EB: O_2 = 10$, carbon balance at 100 ± 5 %.

conditions could last for over 20 hs, and the XRD and HR-TEM (Fig. S8 and Fig. S9) measurements on the spent catalysts suggested that there is no obvious Pd agglomeration, indicating the high stability of Pd@HNSs in DPDH reaction route. The Pd content of used Pd@HNSs after DPDH from ICP and XPS were 0.47 wt% and 0.86 wt% respectively, which were similar to that before DPDH reaction. The similar Pd content before and after DPDH reaction indicates that there is no obvious Pd leaching or coke deposition on Pd@HNSs after DPDH. The ST formation rate on Pd@HNSs in DPDH process reached $7.11 \text{ mmol g}^{-1} \text{ h}^{-1}$ under the optimized reaction conditions (12 kPa EB, 1.2 kPa O_2) surpassing other typical reported ST synthesis reaction systems (Fig. S10 and Table S4), showing its great potential for future practical applications for ST synthesis.

3.3. Reaction mechanism and dehydrogenation activity enhancement via water assistance

The detailed reaction path and the physical-chemical nature behind the high activity of EB DPDH on Pd@HNSs catalysts were unraveled in this part via *in situ* FT-IR, temperature programmed surface reaction (TPSR) with on-line mass spectrometer detectors and theoretical calculations. Fig. S11a showed the *in situ* FT-IR spectra for TPSR during DPDH process, revealing the evolution of oxygen functionalities during EB DPDH process. The stretching vibration of C-H (ethyl branch) at $2880\text{--}2980 \text{ cm}^{-1}$ demonstrated the interaction (or reaction) of ethyl branch from EB with the Pd@HNSs catalysts [44]. A new vinyl overtone peak appeared with the reaction temperature elevated over 200°C , corresponding to the formation of surface ST species [45]. At the same time, the intensity of $\text{C}=\text{O}$ signal at 1650 cm^{-1} decreased, while the $-\text{OH}$ band at 3200 cm^{-1} enhanced correspondingly, suggesting the partial reduction of Pd@HNSs and the formation of ST [44,45]. The activation of EB on $\text{C}=\text{O}$ sites could also be observed from the *in situ* FT-IR spectra (Fig. S11b) for DPDH under the catalysis of Pd@HNSs at 500°C as a function of the reaction time. The characteristic signal belonging to $-\text{OH}$ emerged after feeding the reactant (EB and O_2) for

1 min, while the IR band of H_2O ($3530\text{--}3780 \text{ cm}^{-1}$) appeared after feeding the reactant for 3 mins, lagging behind the $-\text{OH}$ band, which may suggest that the $-\text{OH}$ groups are re-oxidized with the assistance of O_2 by releasing H_2O . This reduction-reoxidation process was further verified by the control experiment with ^{18}O isotope ($^{18}\text{O}_2$) oxidizing the spent Pd@HNSs (Pd@HNSs after DPDH for 20 hs), and the reactant and product during this process could also be monitored via *in situ* on-line MS measurement. As shown in Fig. 4a, $^{18}\text{O}_2$ would be totally consumed in the first 18 mins (no oxygen molecules came out during this period), demonstrating the relatively strong activation ability of Pd@HNSs for oxygen molecules. The reoxidation product H_2^{16}O formed immediately upon the introduction of $^{18}\text{O}_2$ and the formation rate and quantity of H_2^{16}O even exceeded that of H_2^{18}O during the first 15 min, which should be originated from the reoxidation of hydroxyl groups ($-\text{OH}$) on the reduced catalysts. H_2^{18}O formed after feeding $^{18}\text{O}_2$ for 15 mins, and the formation rate and quantity of H_2^{16}O and H_2^{18}O were almost identical after that due to the rapid exchange of the gas-phase oxygen and surface oxygen species. A small amount of $^{16}\text{O}_2$ and $^{16}\text{O}^{18}\text{O}$ could also be observed during this process, which demonstrated that the oxygen molecules may first dissociate (activate) on the catalyst surface, and this dissociative adsorption may be a reversible process [44]. The FT-IR and MS results suggested that $\text{C}=\text{O}$ groups on carbon may act as active sites to catalyze EB ODH in DPDH route with the reversible transformation of $\text{C}=\text{O}$ to $-\text{OH}$ with the assistance of O_2 . The relatively high reduction-reoxidation ability of $\text{C}=\text{O}$ enhanced the ST formation rate via ODH route, while this route was limited by low O_2 partial pressure to ensure the ST selectivity.

It is interesting to observe in Fig. 4b that the DDH process on Pd@HNSs catalyst will be enhanced after introducing O_2 , since the lower formation temperature (330 vs. 370°C) and higher amount of H_2 can be clearly observed in DPDH process. On the contrary, production amount of H_2 on HNSs catalyst kept the same in both DDH and DPDH process, which suggested that introducing O_2 will not influence the DDH process, and EB DDH and ODH are two independent reaction processes on HNSs (Fig. 4c). The improvement of EB conversion rate on HNSs in

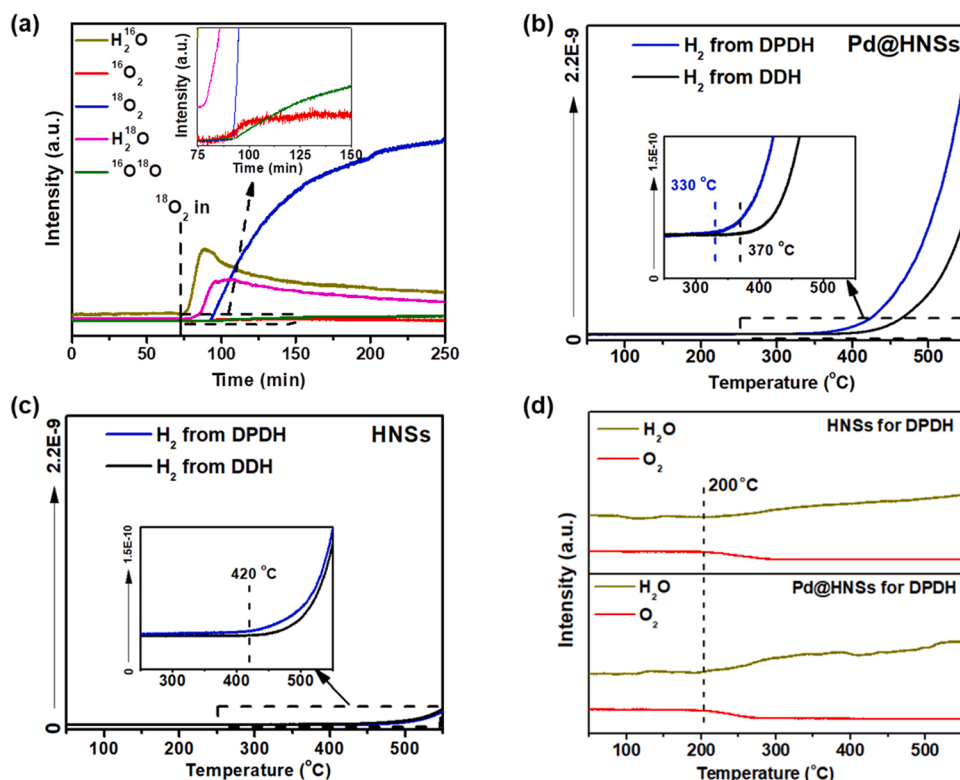


Fig. 4. (a) On-line MS signals during DPDH reaction on the used Pd@HNSs upon the introduction of $^{18}\text{O}_2$ as a function of reaction time. On-line MS signal of (b-c) H_2 and (d) H_2O and O_2 of DPDH and DDH on HNSs and Pd@HNSs as a function of reaction temperature. Reaction conditions for the $^{18}\text{O}_2$ on-line mass spectroscopic measurement: 75 mg catalyst, 300°C , 1.0 kPa $^{18}\text{O}_2$ balanced with He, total flow rate at 7.65 mL/min. DDH conditions for on-line mass spectroscopy: 75 mg catalyst, heating rate at $5^\circ\text{C}/\text{min}$ from 50 to 550°C , 1.0 kPa EB balanced with He, total flow rate at 7.65 mL/min. DPDH conditions for on-line mass spectroscopy: all the reaction conditions were kept the same as DDH except for co-feeding O_2 at EB: $\text{O}_2 = 10$.

DPDH route stems actually from the additional ODH contributions. The consumption of O_2 on HNSs and Pd@HNSs catalysts both started from 200 °C, and the formation amount of H_2O were also almost the same. This means that the ODH process in DPDH route on the two catalysts may follow the same reaction mechanism (Fig. 4d), suggesting EB ODH may mainly happen on HNSs. In contrast, production of H_2 started from 420 °C on HNSs via DDH route, while it started from 370 °C on Pd@HNSs, indicating that DDH reaction mechanism on these two catalysts may be different. It is easy to understand this point that Pd single atom exhibits high reactivity for C-H bond activation during alkane DDH reactions [46]. DDH reactions mainly happen on Pd single atom sites on Pd@HNSs. It can also be observed that the H_2 production temperature

further down shifted by 40 °C to 330 °C in the presence of small amount of O_2 (DPDH route), suggesting the ODH reaction may benefit to DDH process on Pd@HNSs. This should be partially attributed to the exothermic nature of ODH reaction providing extra thermal energy to compensate the heat requirement of endothermic DDH reaction [47,48]. More importantly, the H_2O that are in situ produced via ODH route has profound promotion effect on the DDH process, which can be testified via both DFT calculation and experimental observations.

The physical chemical nature of DPDH reaction route on PdN₃-Gr and especially the H_2O assisted H_2 desorption process was simulated by DFT calculations, and the corresponding computed energy profiles were shown in Fig. 5. The adsorption energy of EB on PdN₃-Gr was observed

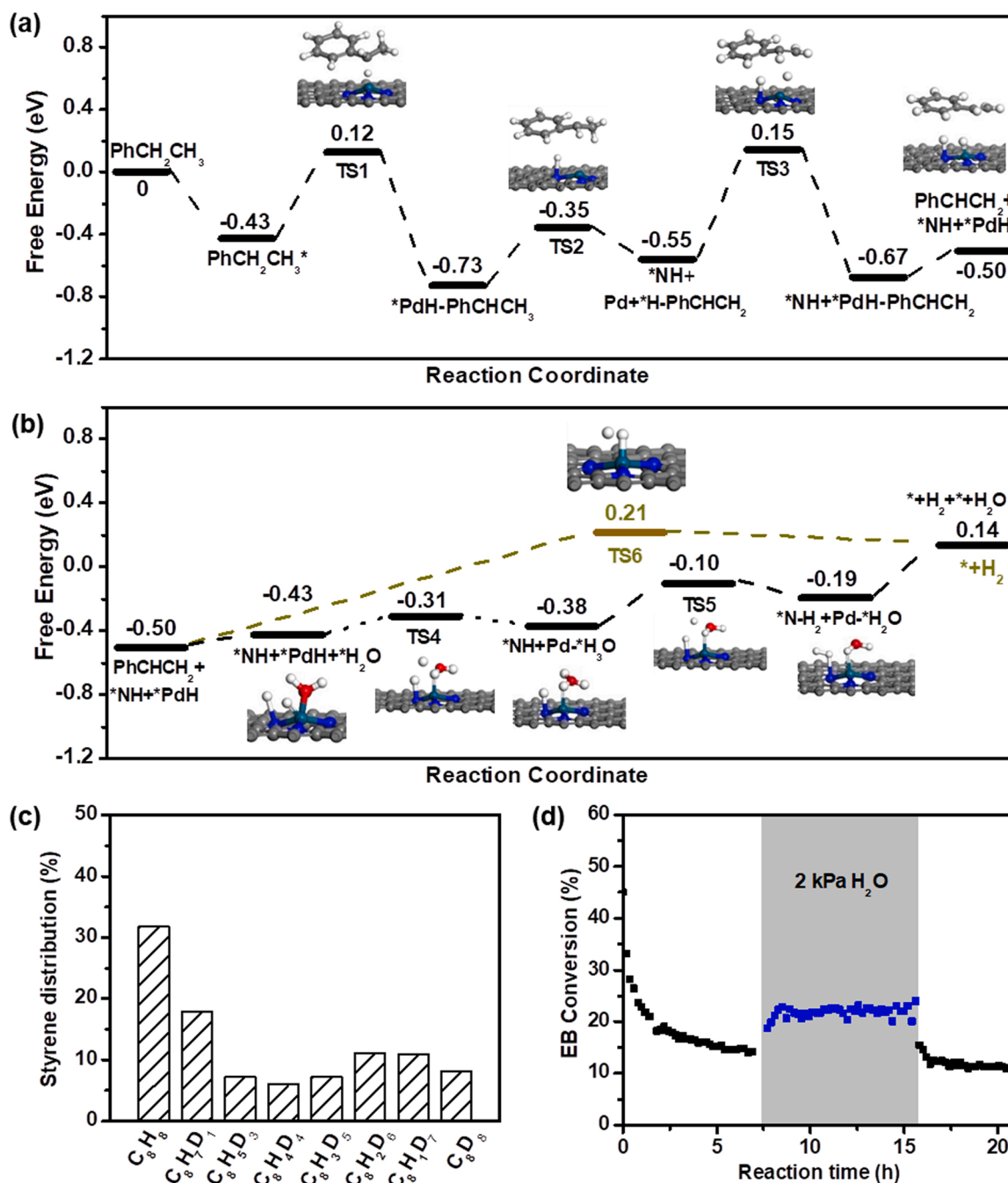


Fig. 5. Computed energy profile of (a) EB dehydrogenation to ST and (b) water assisted proton transfer and H_2 desorption on Pd@HNSs. (c) Styrene isotopes distribution of DPDH on Pd@HNSs upon co-feeding of EB and D-EB. Reaction conditions for on-line mass spectroscopy: 75 mg catalyst, 500 °C, co-feeding of EB and D-EB at 1.0 kPa (EB:D-EB=1:1), EB: O_2 = 10, total flow rate at 7.65 mL/min balanced with He. (d) EB conversion as a function of reaction time on Pd@HNSs with co-feeding H_2O at 7.5–15.5 h. Reaction conditions: 50 mg catalyst, 500 °C, 2 kPa EB, total flow rate at 7.65 mL/min balanced with He, 2 kPa H_2O at 7.5–15.5 h.

at -0.43 eV, suggesting it is a spontaneous process. The computed activation energies for α and β hydrogen abstraction from EB (0.12 and 0.15 eV) were much lower than those reported over other typical catalysts for C-H bond activation, such as V_2O_5 (1.96 and 2.23 eV) [49] and $-C=O$ on nanocarbon (0.84 and 0.79 eV) etc. [50], showing the admirable C-H bond activation ability for the synthesized PdN_3 structure, which could be demonstrated by the isotope control experiment via co-feeding C_6H_{10} and C_6D_{10} (Fig. 5c). The product styrene isotopes possess various amount of D substitution from 1 to 8, suggesting the high activity of C-H/D bond activation and H/D exchange on the surface of $Pd@HNSs$ [45]. The energy barrier for the hydrogen abstraction from β -C was determined at 0.70 eV, which was higher than that for sequential hydrogen abstraction from α -C (0.55 eV). This result suggested the abstraction of β -hydrogen may be the rate-determining step for EB DDH, which is in accordance with KIE result in Fig. 3d. Following the abstraction of α and β hydrogen, the generated ST readily desorbed from the PdN_3 -Gr with favorable energy barrier, which is consistent with the high selectivity observed from the experimental results. Meanwhile, the two abstracted H atoms left on the PdN_3 -Gr coordinated with nitrogen and Pd centers in the forms of N-H and Pd-H, which desorbed subsequently as H_2 completing the reaction cycle. This process was found highly endothermic with the energy barrier of 0.71 eV (Fig. 5b), which is similar to that for β -H abstraction (0.70 eV), meaning that formation and desorption of H_2 may be kinetically coupled with hydrogen abstraction in DDH process. The effect of small amount of H_2O on EB conversion could be clearly seen in Fig. 5d, in which EB conversion has obvious increase with introducing small amount of H_2O (between 7.5 and 15.5 h), testifying the intrinsic advantage of DPDPH process [45].

In the proposed DPDPH route, the exothermic ODH reaction on $C=O$ groups can not only provide partially the thermal energy to compensate the heat requirement of DDH but also can facilitate the formation of H_2 with the assistance of the formed H_2O . As shown in Fig. 5 b, H_2O molecules yielded from EB ODH would be first chemically adsorbed on Pd via Pd-O bond, and then it abstracted hydrogen atom from Pd-H forming a H_3O^+ -like structure. Finally, the proton of H_3O^+ transferred to N-H releasing H_2 . This H_2O assisted proton transfer and H_2 desorption process exhibits a thermodynamic advantage of 0.33 eV for decreasing the reaction barrier for H_2 formation, revealing the physical-chemical nature of the ODH assisted DDH process and the advantage of the proposed DPDPH process. This promotion effect is similar to that observed on FeO thin film [51] and $KFeO_2$ surface [45], and it is also well consistent with the observations in control experiment for co-feeding H_2O as shown in Fig. 5d. According to above results, we proposed a mechanistic diagram for the DPDPH process over $Pd@HNSs$ catalyst as shown in Fig. S12. These mechanistic findings, including the DDH reaction pathway and the promotion of H_2O on hydrogen formation, which were testified by both experiments and DFT calculations, provided important insights/-guidelines for the rational design of the catalysts and reaction conditions towards highly efficient ST synthesis.

4. Conclusions

In summary, we have proposed a dual-path dehydrogenation reaction of EB on bifunctional $Pd@HNSs$ hybrid catalysts for highly efficient ST synthesis. Pd single-atoms and quinone groups serve as active sites for EB DDH and ODH respectively. The dual-path dehydrogenation is not only the simple sum but also the synergy between DDH and ODH process, leading to relatively high ST formation rate. First, the high surface area, highly dispersed active sites and stable single atomic Pd species enable $Pd@HNSs$ high DDH activity. ODH reactions on $C=O$ group do not only provide the energy to compensate the heat requirement of endothermic DDH process but also yield small amount of H_2O that can lower the energy barrier for H_2 formation and desorption via a proton transfer process as evidenced by experimental observations and DFT calculations. The present study provides a novel DPDPH route for

alkane dehydrogenation, shedding light on the rational design of carbon-based dehydrogenation catalysts and proper choice of reaction conditions for boosted styrene synthesis efficiency.

CRedit authorship contribution statement

Xueya Dai: Research plan, Data processing, Investigation, Software, Writing – original draft. **Tianlong Cao:** Validation, Writing – review & editing. **Xingyu Lu:** Validation, Writing – review & editing. **Yunli Bai:** Validation, Writing – review & editing. **Wei Qi:** Funding acquisition, Validation, Writing – review & editing.

Declaration of Competing Interest

The authors declare that they have no known competing financial interests or personal relationships that could have appeared to influence the work reported in this paper.

Data availability

Data will be made available on request.

Acknowledgements

The authors acknowledge the financial support from the NSFC of China (22072163), the Natural Science Foundation of Liaoning Province of China (2020-YQ-02) and China Baowu Low Carbon Metallurgy Innovation Foundation BWLCF202113.

Appendix A. Supporting information

Supplementary data associated with this article can be found in the online version at doi:10.1016/j.apcatb.2022.122205.

References

- [1] I. Kainthla, J.T. Bhanushali, R.S. Keri, B.M. Nagaraja, Activity studies of vanadium, iron, carbon and mixed oxides based catalysts for the oxidative dehydrogenation of ethylbenzene to styrene: a review, *Catal. Sci. Technol.* 5 (2015) 5062–5076.
- [2] Z. Hong, C. Xiong, G. Zhao, Z. Zhu, Side-chain alkylation of toluene with methanol to produce styrene: an overview, *Catal. Sci. Technol.* 9 (2019) 6828–6840.
- [3] Z. Luo, Q. Wan, Z. Yu, S. Lin, Z. Xie, X. Wang, Photo-fluorination of nanodiamonds catalyzing oxidative dehydrogenation reaction of ethylbenzene, *Nat. Commun.* 12 (2021) 6542.
- [4] S.K. Kaiser, Z. Chen, D. Faust Akl, S. Mitchell, J. Perez-Ramirez, Single-atom catalysts across the periodic table, *Chem. Rev.* 120 (2020) 11703–11809.
- [5] Y. Ying, X. Luo, J. Qiao, H. Huang, “More is Different”: synergistic effect and structural engineering in double-atom catalysts, *Adv. Funct. Mater.* 31 (2020), 2007423.
- [6] L. Liu, A. Corma, Confining isolated atoms and clusters in crystalline porous materials for catalysis, *Nat. Rev. Mater.* 6 (2020) 244–263.
- [7] H. Zhou, X. Yi, Y. Hui, L. Wang, W. Chen, Y. Qin, M. Wang, J. Ma, X. Chu, Y. Wang, X. Hong, Z. Chen, X. Meng, H. Wang, Q. Zhu, L. Song, A. Zheng, F.S. Xiao, Isolated boron in zeolite for oxidative dehydrogenation of propane, *Science* 372 (2021) 76–80.
- [8] X.-L. Xue, W.-Z. Lang, X. Yan, Y.-J. Guo, Dispersed vanadium in three-dimensional dendritic mesoporous silica nanospheres: active and stable catalysts for the oxidative dehydrogenation of propane in the presence of CO_2 , *ACS Appl. Mater. Interfaces* 9 (2017) 15408–15423.
- [9] Z. Maeno, S. Yasumura, X. Wu, M. Huang, C. Liu, T. Toyao, K.I. Shimizu, Isolated indium hydrides in CHA zeolites: speciation and catalysis for nonoxidative dehydrogenation of ethane, *J. Am. Chem. Soc.* 142 (2020) 4820–4832.
- [10] Y. Xiong, W. Sun, Y. Han, P. Xin, X. Zheng, W. Yan, J. Dong, J. Zhang, D. Wang, Y. Li, Cobalt single atom site catalysts with ultrahigh metal loading for enhanced aerobic oxidation of ethylbenzene, *Nano. Res.* 14 (2021) 2418–2423.
- [11] Y. Han, Z. Wang, R. Xu, W. Zhang, W. Chen, L. Zheng, J. Zhang, J. Luo, K. Wu, Y. Zhu, C. Chen, Q. Peng, Q. Liu, P. Hu, D. Wang, Y. Li, Ordered porous nitrogen-doped carbon matrix with atomically dispersed cobalt sites as an efficient catalyst for dehydrogenation and transfer hydrogenation of N-heterocycles, *Angew. Chem. Int. Ed. Engl.* 57 (2018) 11262–11266.
- [12] H. Xiong, S. Lin, J. Goetze, P. Pletcher, H. Guo, L. Kovarik, K. Artyushkova, B. M. Weckhuysen, A.K. Datye, Thermally stable and regenerable platinum-tin clusters for propane dehydrogenation prepared by atom trapping on Ceria, *Angew. Chem. Int. Ed. Engl.* 56 (2017) 8986–8991.

- [13] S. Barman, N. Maity, K. Bhatte, S. Ould-Chikh, O. Dachwald, C. Haeßner, Y. Saih, E. Abou-Hamad, I. Llorens, J.-L. Hazemann, K. Köhler, V. D'Elia, J.-M. Basset, Single-site VOx moieties generated on silica by surface organometallic chemistry: a way to enhance the catalytic activity in the oxidative dehydrogenation of propane, *ACS Catal.* 6 (2016) 5908–5921.
- [14] K. Searles, G. Siddiqi, O.V. Safonova, C. Coperet, Silica-supported isolated gallium sites as highly active, selective and stable propane dehydrogenation catalysts, *Chem. Sci.* 8 (2017) 2661–2666.
- [15] T. Cao, X. Dai, F. Li, W. Liu, Y. Bai, Y. Fu, W. Qi, Efficient non-precious metal catalyst for propane dehydrogenation: atomically dispersed cobalt-nitrogen compounds on carbon nanotubes, *ChemCatChem* 13 (2021) 3067–3073.
- [16] J. Shan, J. Liu, M. Li, S. Lustig, S. Lee, M. Flytzani-Stephanopoulos, NiCu single atom alloys catalyze the C-H bond activation in the selective non-oxidative ethanol dehydrogenation reaction, *Appl. Catal. B Environ.* 226 (2018) 534–543.
- [17] J. Zhang, X. Liu, R. Blume, A. Zhang, R. Schlögl, D.S. Su, Surface-modified carbon nanotubes catalyze oxidative dehydrogenation of n-butane, *Science* 322 (2008) 73–77.
- [18] W. Liu, C. Wang, F. Herold, B.J.M. Etzold, D. Su, W. Qi, Oxidative dehydrogenation on nanocarbon: effect of heteroatom doping, *Appl. Catal. B Environ.* 258 (2019), 117982.
- [19] J. Zhang, R. Wang, E. Liu, X. Gao, Z. Sun, F.S. Xiao, F. Girgsdies, D.S. Su, Spherical structures composed of multiwalled carbon nanotubes: formation mechanism and catalytic performance, *Angew. Chem. Int. Ed. Engl.* 51 (2012) 7581–7585.
- [20] X. Huang, H. Yan, L. Huang, X. Zhang, Y. Lin, J. Li, Y. Xia, Y. Ma, Z. Sun, S. Wei, J. Lu, Toward understanding of the support effect on Pd1 single-atom-catalyzed hydrogenation reactions, *J. Phys. Chem. C* 123 (2018) 7922–7930.
- [21] Y. Lin, D. Su, Fabrication of nitrogen-modified annealed nanodiamond with improved catalytic activity, *ACS Nano* 8 (2014) 7823–7833.
- [22] X. Sun, Y. Ding, B. Zhang, R. Huang, D.S. Su, New insights into the oxidative dehydrogenation of propane on borate-modified nanodiamond, *Chem. Commun.* 51 (2015) 9145–9148.
- [23] X. Sun, Y. Ding, B. Zhang, R. Huang, D. Chen, D.S. Su, Insight into the enhanced selectivity of phosphate-modified annealed nanodiamond for oxidative dehydrogenation reactions, *ACS Catal.* 5 (2015) 2436–2444.
- [24] P. Yan, X. Zhang, F. Herold, F. Li, X. Dai, T. Cao, B.J.M. Etzold, W. Qi, Methanol oxidative dehydrogenation and dehydration on carbon nanotubes: active sites and basic reaction kinetics, *Catal. Sci. Technol.* 10 (2020) 4952–4959.
- [25] R. Li, D. Wang, Understanding the structure-performance relationship of active sites at atomic scale, *Nano. Res.* 15 (2022) 6888–6923.
- [26] G. Kresse, J. Furthmüller, Efficiency of ab-initio total energy calculations for metals and semiconductors using a plane-wave basis set, *Comput. Mater. Sci.* 6 (1996) 15–50.
- [27] G. Kresse, J. Furthmüller, Efficient iterative schemes for ab initio total-energy calculations using a plane-wave basis set, *Phys. Rev. B Condens. Matter* 54 (1996) 11169–11186.
- [28] J.P. Perdew, K. Burke, M. Ernzerhof, Generalized gradient approximation made simple, *Phys. Rev. Lett.* 77 (1996) 3865–3868.
- [29] G. Kresse, D. Joubert, From ultrasoft pseudopotentials to the projector augmented-wave method, *Phys. Rev. B* 59 (1999) 1758–1775.
- [30] P.E. Blochl, Projector augmented-wave method, *Phys. Rev. B Condens. Matter* 50 (1994) 17953–17979.
- [31] L. Peng, C.-T. Hung, S. Wang, X. Zhang, X. Zhu, Z. Zhao, C. Wang, Y. Tang, W. Li, D. Zhao, Versatile nanoemulsion assembly approach to synthesize functional mesoporous carbon nanospheres with tunable pore sizes and architectures, *J. Am. Chem. Soc.* 141 (2019) 7073–7080.
- [32] S. Zeng, G.M. Arumugam, X. Liu, Y. Yang, X. Li, H. Zhong, F. Guo, Y. Mai, Encapsulation of sulfur into N-doped porous carbon cages by a facile, template-free method for stable lithium-sulfur cathode, *Small* (2020), e2001027.
- [33] S. Tian, P. Yan, F. Li, X. Zhang, D. Su, W. Qi, Fabrication of polydopamine modified carbon nanotube hybrids and their catalytic activity in ethylbenzene dehydrogenation, *ChemCatChem* 11 (2019) 2073–2078.
- [34] A. Han, W. Chen, S. Zhang, M. Zhang, Y. Han, J. Zhang, S. Ji, L. Zheng, Y. Wang, L. Gu, C. Chen, Q. Peng, D. Wang, Y. Li, A Polymer encapsulation strategy to synthesize porous nitrogen-doped carbon-nanosphere-supported metal isolated-single-atomic-site catalysts, *Adv. Mater.* 30 (2018), e1706508.
- [35] C. Zhao, H. Yu, J. Wang, W. Che, Z. Li, T. Yao, W. Yan, M. Chen, J. Yang, S. Wei, Y. Wu, Y. Li, A single palladium site catalyst as a bridge for converting homogeneous to heterogeneous in dimerization of terminal aryl acetylenes, *Mater. Chem. Front.* 2 (2018) 1317–1322.
- [36] S. Büchele, Z. Chen, S. Mitchell, R. Hauert, F. Krumeich, J. Pérez-Ramírez, Tailoring nitrogen-doped carbons as hosts for single-atom catalysts, *ChemCatChem* 11 (2019) 2812–2820.
- [37] L. Han, Z. Ren, P. Ou, H. Cheng, N. Rui, L. Lin, X. Liu, L. Zhuo, J. Song, J. Sun, J. Luo, H.L. Xin, Modulating single-atom palladium sites with copper for enhanced ambient ammonia electrosynthesis, *Angew. Chem. Int. Ed. Engl.* 60 (2021) 345–350.
- [38] X. Liu, X. Zhai, W. Sheng, J. Tu, Z. Zhao, Y. Shi, C. Xu, G. Ge, X. Jia, Isolated single iron atoms anchored on a N, S-codoped hierarchically ordered porous carbon framework for highly efficient oxygen reduction, *J. Mater. Chem. A* 9 (2021) 10110–10119.
- [39] X. Zhu, D. Zhang, C.-J. Chen, Q. Zhang, R.-S. Liu, Z. Xia, L. Dai, R. Amal, X. Lu, Harnessing the interplay of Fe-Ni atom pairs embedded in nitrogen-doped carbon for bifunctional oxygen electrocatalysis, *Nano Energy* 71 (2020), 104597.
- [40] K. Wu, F. Zhan, R. Tu, W.C. Cheong, Y. Cheng, L. Zheng, W. Yan, Q. Zhang, Z. Chen, C. Chen, Dopamine polymer derived isolated single-atom site metals/N-doped porous carbon for benzene oxidation, *Chem. Commun.* 56 (2020) 8916–8919.
- [41] X. Han, X. Ling, D. Yu, D. Xie, L. Li, S. Peng, C. Zhong, N. Zhao, Y. Deng, W. Hu, Atomically dispersed binary Co-Ni sites in nitrogen-doped hollow carbon nanocubes for reversible oxygen reduction and evolution, *Adv. Mater.* 31 (2019), e1905622.
- [42] W. Qi, W. Liu, B. Zhang, X. Gu, X. Guo, D. Su, Oxidative dehydrogenation on nanocarbon: identification and quantification of active sites by chemical titration, *Angew. Chem. Int. Ed. Engl.* 52 (2013) 14224–14228.
- [43] W. Qi, W. Liu, X. Guo, R. Schlögl, D. Su, Oxidative dehydrogenation on nanocarbon: intrinsic catalytic activity and structure-function relationships, *Angew. Chem. Int. Ed. Engl.* 54 (2015) 13682–13685.
- [44] X. Guo, W. Qi, W. Liu, P. Yan, F. Li, C. Liang, D. Su, Oxidative dehydrogenation on nanocarbon: revealing the catalytic mechanism using model catalysts, *ACS Catal.* 7 (2017) 1424–1427.
- [45] X. Zhu, Y. Gao, X. Wang, V. Haribal, J. Liu, L.M. Neal, Z. Bao, Z. Wu, H. Wang, F. Li, A tailored multi-functional catalyst for ultra-efficient styrene production under a cyclic redox scheme, *Nat. Commun.* 12 (2021) 1329.
- [46] Z. Mao, H. Gu, X. Lin, Recent advances of Pd/C-catalyzed reactions, *Catalysts* 11 (2021) 1078.
- [47] K. Avasthi, A. Bohre, M. Grilc, B. Likozar, B. Saha, Advances in catalytic production processes of biomass-derived vinyl monomers, *Catal. Sci. Technol.* 10 (2020) 5411–5437.
- [48] Q. Zhao, Q. Mao, Y. Zhou, J. Wei, X. Liu, J. Yang, L. Luo, J. Zhang, H. Chen, H. Chen, L. Tang, Metal-free carbon materials-catalyzed sulfate radical-based advanced oxidation processes: a review on heterogeneous catalysts and applications, *Chemosphere* 189 (2017) 224–238.
- [49] H. Fan, J. Feng, X. Li, Y. Guo, W. Li, K. Xie, Ethylbenzene dehydrogenation to styrene with CO₂ over V₂O₅ (001): a periodic density functional theory study, *Chem. Eng. Sci.* 135 (2015) 403–411.
- [50] Z. Lian, C. Si, F. Jan, M. Yang, B. Li, Resolving the mechanism complexity of oxidative dehydrogenation of hydrocarbons on nanocarbon by microkinetic modeling, *ACS Catal.* 10 (2020) 14006–14014.
- [51] L.R. Merte, G. Peng, R. Bechstein, F. Rieboldt, C.A. Farberow, L.C. Grabow, W. Kudernatsch, S. Wendt, E. Laegsgaard, M. Mavrikakis, F. Besenbacher, Water-mediated proton hopping on an iron oxide surface, *Science* 336 (2012) 889–893.